Radiation Effects & Defects in Solids: Incorporating Plasma Science & Plasma Technology
Vol. 165, No. 4, April 2010, 265–276

Defect engineering and opto electronic property modifications by 1.5 MeV Li^+ implantation on nano crystalline $MgIn_2O_4$ thin films

A. Moses Ezhil Raj[a], T. Som[b], M. Jayachandran[c] and C. Sanjeeviraja[d]*

[a]*Department of Physics, Scott Christian College (Autonomous), Nagercoil 629 003, India;* [b]*Institute of Physics, Bhubaneswar 751 005, India;* [c]*ECMS Division, Central Electrochemical Research Institute, Karaikudi 630 006, India;* [d]*Department of Physics, Alagappa University, Karaikudi 630 003, India*

(*Received 12 November 2009; final version received 18 January 2010*)

Spinel $MgIn_2O_4$ thin films were deposited on quartz substrates by the chemical spray pyrolysis technique using metal organic precursors at 450°C. Energetic 1.5 MeV Li^+ ions were implanted to various fluences of 10^{13}, 10^{14} and 10^{15} ions/cm^2 onto insulating $MgIn_2O_4$ films using a 9 SDH-2, NEC, 3MV accelerator to modify the material properties and surface nature. X-ray diffraction analysis was carried out to identify the changes in the crystallinity and grain orientations before and after implantations. Before implantation, the grains of polycrystalline $MgIn_2O_4$ were randomly oriented [(222), (311), (442) and (511)], and after implantation they exhibited a tendency to realign the crystallites along the even (*hkl*) planes [(222) and (442)]. On the Li^+-implanted sample, one or more grains combine together and form bigger grains along with shallow pits, as observed through the atomic force micrographs. The as-deposited films have a percentage transmittance of 70–80% in the wavelength range 400–800 nm and the observed optical transmittance was less in Li^+-implanted $MgIn_2O_4$ films. The index of refraction and the extinction co-efficient values were respectively $n = 1.98$ and $k = 10^{-2}$ in the visible region. However, the DC electrical conductivity of Li^+-implanted films to a fluence of 10^{15} ions/cm^2 was nearly 0.7 S/cm at room temperature. The efficiency of the carrier generation was increased from 13.41% to 26.81% on annealing the implanted sample to lower fluence (10^{13} ions/cm^2).

Keywords: thin films; implantation; X-ray diffraction; optical property; electrical conductivity

PACS: 77.55.+f; 78.70.−g; 61.10.Nz; 78.20.−e; 72.20.−i

1. Introduction

Ion implantation has been used extensively to modify the near-surface structure of crystalline IV and III–V group semiconductors (*1*). Mechanical, physical, or chemical surface-related properties can be beneficially altered by implanting metal ions for numerous applications. Introduction of metal colloids into any transparent material matrix has long been used for fabricating optical filters and transparent electrodes in LCDs and solar cells (*2*, *3*). Indium oxide (In_2O_3, $E_g \sim 3.67$ eV) is one of the wide gap transparent semiconductors and has been used as the window layer of

*Corresponding author. Email: sanjeeviraja@rediffmail.com

ISSN 1042-0150 print/ISSN 1029-4953 online

DOI: 10.1080/10420151003636869
http://www.informaworld.com

solar cells (*4, 5*). The solid solution of In_2O_3 containing another wide gap material resulting in a new wider band gap material is a tailoring method in semiconductor engineering to instigate elite optoelectronic properties. A suitable candidate for such counter material is magnesium oxide (MgO, $E_g \sim 7.7$ eV) (*6*). Owing to the similarity of the ionic radius between Mg^{2+} (0.57 Å) (*7*) and In^{3+} (0.80 Å) (*8*), the spinel $MgIn_2O_4$ thin films can be obtained without much difficulty. Usually, nanocrystalline films of $MgIn_2O_4$ can be synthesized with Mg excess composition for which the Mg^{2+} ions are occupying the octahedral sites of the spinel lattice (*9*). However, In^{3+} is the dominant factor in determining the cation distribution in $MgIn_2O_4$ due to the small octahedral site preference energy of In^{3+} (−40 kcal/g atomic weight) (*10*).

$MgIn_2O_4$ has a wide optical band gap (>3.5 eV) and hence is transparent, but it is also an electrical insulator. By successful metal doping, insulating oxides can be converted into conductors by increasing the mobility of the electrons by modifying the curvature of the conduction band bottom. This is possible in $MgIn_2O_4$, because of the available vacant 5s orbital of In ions in the dispersed conduction band and the short In–In distances originating from the edge-shared mode of the InO_6 octahedra, which make the effective mass of electrons small (*11*). When the central cations in the octahedra have widely spread unoccupied ns orbitals, large overlap occurs between the ns orbitals and this overlap leads to large dispersion of the conduction band. The optical transparency is therefore due to the wide energy gap, and the high electrical conductivity is due to a highly dispersed s-type band at the bottom of the conduction band (*12*); consequently, $MgIn_2O_4$ can be considered a promising transparent conducting oxide and magnetic superconductor (*13, 14*).

Moreover, a spinel structure has many vacant tetrahedral and octahedral cation sites, which could be available for impurity doping. Since spinels are resistant to radiation damage, the vacant sites can be filled by ions of small ionization potential, size and mass suitable for the vacant sites in the host lattice. In addition, ion implantation modifies the mechanical properties due to the arousal of the tensile component of the applied load that produces stresses that are usually compressive and biaxial in the plane of the sample surface; thus, the effect of the tensile component is reduced, and as a result, the strength of the material is raised.

Based on our work on ion implantation on oxide thin films (*15–17*), we propose a criterion to exhibit exceptional electrical and optical properties in the crystal structure. The crystal structure of the spinel oxide should permit the exchange of ions on lattice sites. The binary oxide spinel also satisfies this criterion, but there is a scarcity of oxides that share good characteristics. This observation leads to search/selection of oxides for good optoelectronic properties that might appeal to design engineers. $MgIn_2O_4$ spinel thin films are selected as a host sample for Li^+ ion implantation, because of its small ionization potential and it being smaller in size, suitable for the tetrahedral sites and a small mass, which are advantages to avoid nuclear collision damage in the host lattice during the implantation. In the study presented here, the effects of implantation of Li^+ ions on $MgIn_2O_4$ thin films and their impact on structural, optical and electrical properties are briefed.

2. Experimental

Magnesium indium oxide films were prepared by dissolving magnesium acetate [$Mg(CH_3COO)_2$ $4H_2O$] and indium chloride ($InCl_3$) in 100% ethanol for the cationic ratio 0.5 (Mg/In). A small amount of concentrated HCl was added to dissolve the salts without any precipitation and to make the solution clear. The solution was then sprayed onto the heated fused quartz (grade 214LD) substrates, which undergo thermal decomposition in the temperature range 400–450 °C. After many trials, the preparative parameters of the system, viz. solution concentration, spray rate, quantity of solution sprayed, substrate–nozzle distance, carrier gas pressure, etc., were optimized to obtain uniform, pin-hole-free and adherent films. The optimized deposition conditions are listed in Table 1.

Table 1. Optimized spray deposition conditions for preparing spinel $MgIn_2O_4$ films.

Spray parameters	Values/quantity
Solvent	100% ethanol
Substrate temperature	400–450°C
Carrier gas flow rate	0.4 kg/cm^2
Substrate to nozzle distance	30 cm
Time of deposition	10 min
Precursor flow rate	5 ml/min

Prior to implantation, thicknesses of the prepared $MgIn_2O_4$ thin film samples were measured using a Mitutoya Surftest SJ-301 Stylus profilometer and they were recorded to be 0.82 μm. Then the samples were irradiated with 1.5 MeV Li^+ ions at room temperature at the Ion Beam Laboratory, Bhubaneswar, India. Initially, samples were loaded in the multifaceted sample holder that was placed inside the irradiation chamber, evacuated to a base pressure of 10^{-8} torr. Then lithium ions were accelerated in a 9 SDH-2, NEC, 3MV accelerator and were allowed to fall on the desired area of the sample. In the present study, an ion beam area of 1×1 cm^2 was maintained for all the samples. During implantation, a single acceleration voltage of 1.5 MeV has been used for Li^+ ions. Electrical contacts were made between the film surface and the holder with carbon tape to avoid charging. In each implantation, the fluence and dose rates were ranged from 10^{13} to 10^{15} ions/cm^2 and 5–10 nA, respectively.

Initially, the projected range of 1.5 MeV Li^+ ions were estimated to be 2.41 μm from TRIM simulations (*18*) using the bulk density of $MgIn_2O_4$ (6.065 g/cm^3). The longitudinal straggling of 1.5 MeV lithium ions in magnesium indium oxide was calculated to be in the order of nanometers using TRIM. X-ray diffraction (XRD) spectra were recorded in a PANalytical-3040 X'pert Pro diffractometer with CuK α radiation of wavelength 1.5406 A° (θ–2θ scan) in the scanning range of 10–80° (2θ). All the peaks in the diffraction pattern were indexed on the basis of Joint Committee for Powder Diffraction Studies (JCPDS) data. The surface morphology of the films was recorded in the atomic force microscope (Nanoscope-E). A constant scan speed of 0.1 μm/s was used and a constant load was applied to the cantilever. The measurement tip is made of Si_3N_4 with a 0.16 N/m stiffness cantilever. Optical absorption and transmittance analysis were carried out using a UV–Vis–NIR spectrophotometer. DC conductivities and Hall measurements were carried out using a four-point probe and the Van der Pauw method, respectively.

3. Results and discussion

3.1. *Structural analysis*

XRD analysis was performed on the Li^+-implanted $MgIn_2O_4$ samples for various fluences, including the as-deposited thin film, and the spectra are shown in Figure 1. The observation shows that all the peaks could be indexed for $Fd\bar{3}$m space group symmetry of the spinel structure. The unit cell of $MgIn_2O_4$ consists of 56 atoms: 8 Mg atoms on the equipoint 8a; 16 In atoms on the equipoint 16d; and 32 O atoms in a ccp arrangement on equipoint 32e. Usually, upon irradiation, atoms are displaced from their regular lattice site and the spinel structure acquires a disordered appearance, due to which the lattice parameter is reduced by a factor of two. However, this kind of transformation is not observed in the present study and it is believed that Li^+ irradiation has not induced any phase transformation. This is due to the reason that irradiation is facilitated at room temperature, which might have affected lattice recovery and prevented the transformation process in the lattice. Usually, implantations at cryogenic temperature induce phase transformation and are reported for $MgAl_2O_4$ spinel oxide thin films (*19, 20*).

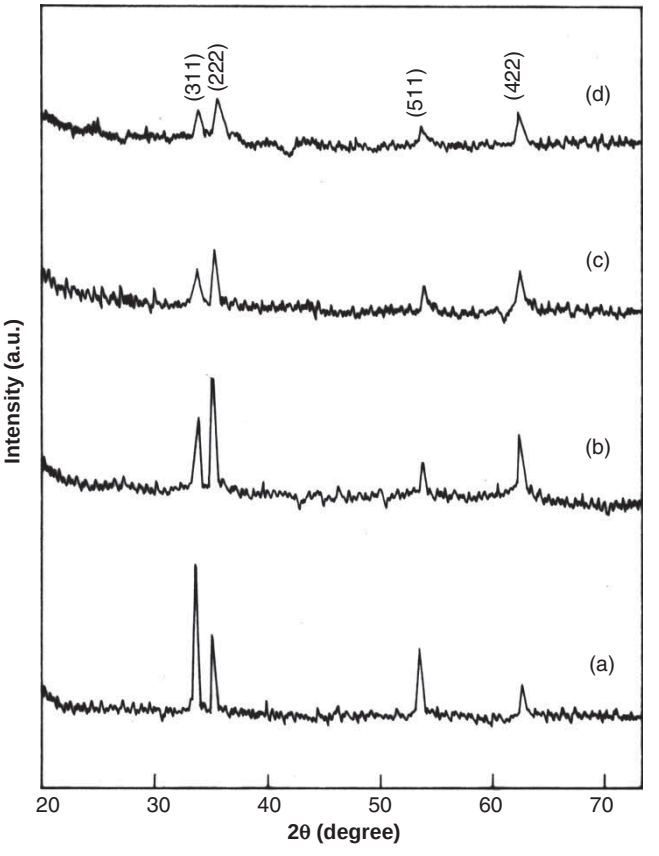

Figure 1. XRD patterns of $MgIn_2O_4$ films (a) as-deposited and Li^+ implanted, (b) 10^{13} ions/cm^2, (c) 10^{14} ions/cm^2 and (d) 10^{15} ions/cm^2.

The radiation resistance of the spinel oxides has been proposed by Sickafus (*21*) and Clinard et al. (*22*). The crystal structure of spinel oxides is complex and has multicomponent chemistry, which in turn suppress the nucleation and growth of interstitial dislocation loops during irradiation. In addition, there is cation exchange that induces a high degree of cation disorder (cation anti-site defects). Also, spinels have an inability of interstitials to condense into planar defects and make interstitial-vacancy recombination. This interstitial-vacancy recombination is a highly efficient point defect annihilation mechanism, and as long as this mechanism is associated with irradiation damage, the radiation resistance of the spinel is assured. However, the XRD peak intensity and peak width are modified depending on ion dosages, but amorphization is not completed and therefore crystallinity has been retained.

Figure 2 shows the XRD peak intensity ratios of Li^+-irradiated $MgIn_2O_4$ samples and those before irradiation as a function of diffraction angle 2θ. Peak intensities of diffraction from (222) and (442) planes for the low irradiated sample (10^{13} ions/cm^2) are observed to increase considerably, when compared with those before irradiation. This suggests that the grains of polycrystalline $MgIn_2O_4$ oriented randomly before irradiation have a tendency to realign the crystallites along the even (*hkl*) planes after irradiation. It is also noted that the increase in the intensity of the (442) peak is larger than that of the (222) peak. However, the peak intensities of all the lines are observed to decrease noticeably with an increase of ion dosages to 10^{14} and 10^{15} ions/cm^2. But, for all irradiation dosages, the intensity of odd (*hkl*) planes, (311) and (511), illustrate a continuous decreasing trend.

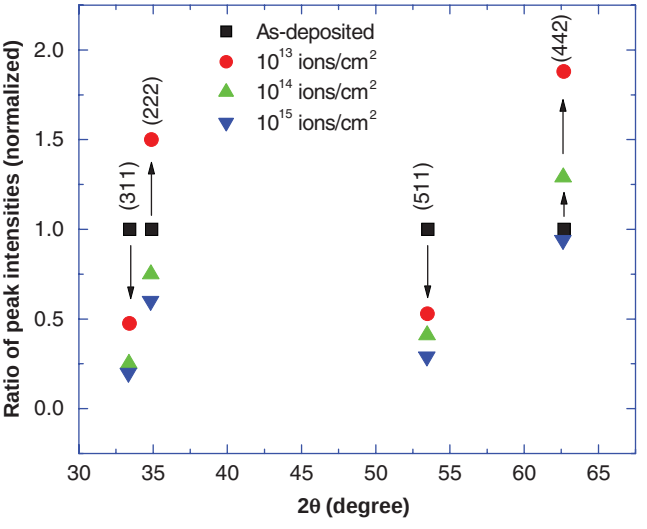

Figure 2. Changes in XRD peak intensity ratio for various implantation dosages.

The structural parameters evaluated for $MgIn_2O_4$ films implanted with different ion fluences are summarized in Table 2. It is noted that the FWHM of all diffraction peaks are increased, irrespective of Li^+ fluences, which in turn reduces the average crystallite size of the irradiated films. The observed crystallite size is different in all the crystallographic planes that reveal the non-spherical nature of the crystallites. The dislocation density and microstrain also gradually increase with irradiation dosage. As the fluence increases, due to a cationic radii effect, O atoms are slightly shifted from (1/4, 1/4, 1/4) to a more general (u, u, u) position, leading to octahedral and tetrahedral distortions (*23*). This leads to an increase in dislocation density and microstrain. The variation of the average lattice parameter and internal stress as a function of fluence is shown in Figure 3.

The exact value of the lattice parameter has been evaluated by the software used for refinement of powder diffraction data – Unit Cell. The refined lattice constant of the unirradiated sample is

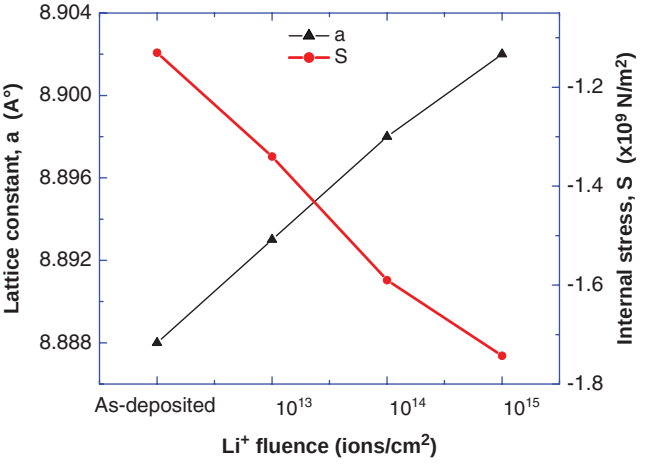

Figure 3. Lattice constant and internal stress of Li^+-irradiated spinel as a function of fluence.

Table 2. Parameters derived from diffraction peaks of Li^+-implanted $MgIn_2O_4$ thin films for various fluences.

Sample details	Diffraction angle (2θ) (degree)	Miller indices (hkl)	d-spacing (Å)		Lattice constant (Å)		FWHM (°)	Crystalline size (D) (nm)	Dislocation density (δ) $\times 10^{14}$ (lines/m^2)	Internal stress (S) $\times 10^9$ (N/m^2)	Micro-strain (ε) $\times 10^{-3}$
			Observed	Standard	Observed	Standard					
As-deposited	33.43	311	2.6785	2.6726	8.887 (2)	8.864	0.16	51.8	3.73	0.903	0.62
	34.91	222	2.568	2.5588			0.2	43.36	5.32	−1.47	0.71
	53.52	511	1.7109	1.7058			0.4	23.16	18.64	−1.2	0.88
	62.69	442	1.4807	1.4773			0.4	23.82	17.61	−0.94	0.74
Li^+ implanted	33.4	311	2.6804	2.6726	8.892 (2)	8.864	0.18	47.06	4.51	−1.19	0.68
10^{13} ions/cm^3	34.88	222	2.5696	2.5588			0.24	35.34	8.01	−1.73	0.87
	53.49	511	1.7116	1.7058			0.54	17.01	34.56	−1.38	1.21
	62.66	442	1.4812	1.4773			0.56	17.2	33.8	−1.07	1.03
Li^+ implanted	33.36	311	2.683	2.6726	8.896 (3)	8.864	0.21	41.09	5.92	−1.6	0.78
10^{14} ions/cm	34.86	222	2.5715	2.5588			0.27	31.47	10.09	−2.03	0.98
	53.47	511	1.712	1.7058			0.58	15.9	39.53	−1.47	1.29
	62.63	442	1.4818	1.4773			0.61	15.81	39.99	−1.24	1.12
Li^+ implanted	33.34	311	2.6846	2.6726	8.899 (3)	8.864	0.32	26.68	14.04	−1.84	1.21
10^{15} ions/cm	34.84	222	2.5729	2.5588			0.36	23.86	17.56	−2.22	1.29
	53.44	511	1.7128	1.7058			0.64	14.33	48.66	−1.62	1.43
	62.62	442	1.482	1.4773			0.68	14.13	50.07	−1.29	1.25

about 8.887 Å. Significant changes are observed in the lattice constant at higher fluences. It attains a value of 8.899 Å at the fluence of 10^{15} ions/cm^2. Owing to the expansion of the unit cell, tensile stress is acting on the unit cell, which also increases with fluence. The grain size of the as-deposited film is decreased from 51.80 to 26.68 nm as the irradiation fluence is increased to 10^{15} ions/cm^2. The decrease in grain size with ion dosage may be due to initiation of amorphization of the films with impaired crystallinity. This in turn has a profound effect on microstrain and dislocation density.

3.2. *Microstructure*

The atomic force microstructural observation on polycrystalline $MgIn_2O_4$ thin film specimens irradiated with 1.5 MeV Li^+ ions to a fluence of 10^{15} ions/cm^2 along with the unimplanted sample is shown in Figure 4. The microstructure of these two specimens is completely different,

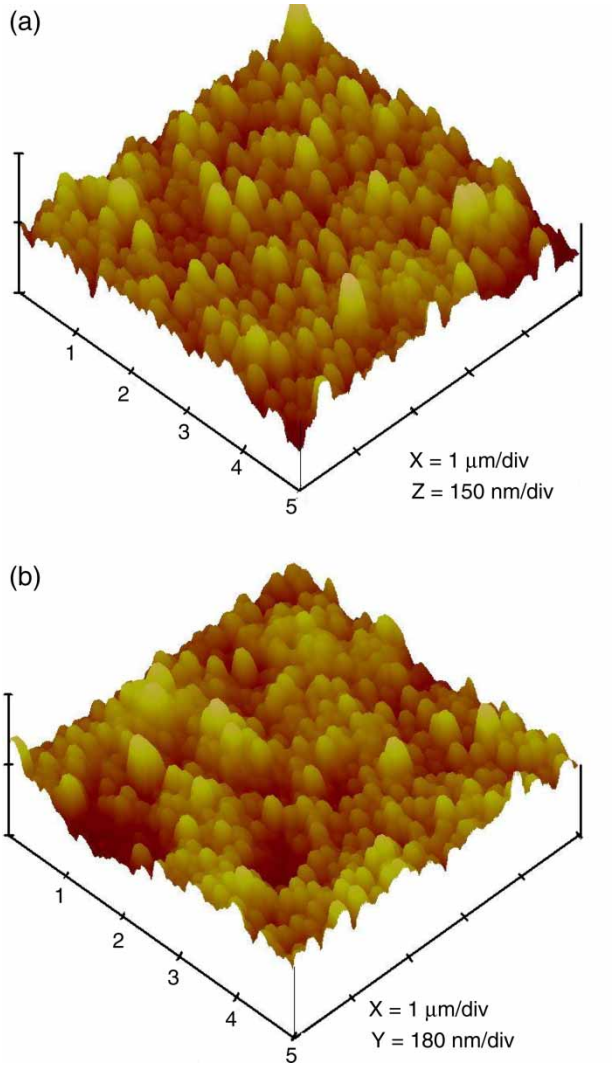

Figure 4. (a) AFM micrographs of the as-deposited $MgIn_2O_4$ films. (b) Micro-structural changes in irradiated spinel oxide with Li^+ ions to a fluence of 10^{15} ions/cm^2.

as evidenced from the figure. The surface of the unimplanted sample is smooth, and shallow pits are not prominent. On the Li^+-implanted sample, recrystallization occurs due to the mobility of the radiation effect and therefore one or more grains combine together and form bigger grains on the surface of the film. However, the overall grain size is less compared with that of the as-deposited films. In addition, the surface is not smooth due to the presence of shallow pits that are developed due to irradiation. Normally, in spinel oxides, ion irradiation yields surface roughening to a large extent (*24*). But amorphization is not observed, as revealed by the XRD studies.

Quantitative analysis of the surface roughness was carried out on large scale images by using the root mean square [RMS(R_q)] function of the Nanoscope III-DI software, to find out the standard deviation of the surface height, calculated from all points obtained during a given scan. The RMS roughness of the $MgIn_2O_4$ films as-deposited at 450 °C was 5.6 nm. However, the RMS roughness of the $MgIn_2O_4$ films implanted to a fluence of 10^{15} Li ions/cm^2 was enhanced to 10.23 nm. These results further confirm the rough surface nature of the ion implanted films.

3.3. *Optical properties*

Figure 5 shows the optical absorption spectra of magnesium indium oxide films implanted with 1.5 MeV Li^+ ions for various fluences of 10^{13}–10^{15} ions/cm^2. The absorption spectrum of unirradiated $MgIn_2O_4$ films is also given for reference in the wavelength range between 200 and 1100 nm. It is inferred that the absorption spectra have three features: the sloping from 300 to 350 nm, strong absorption region at 365 nm and a broadband around 540 nm. The hump at 2.3 eV (540 nm) is ascribed to surface plasmon resonance of Li nanoparticles and the wide slope is due to the transitions from the lithium sublevels including widely spread defect bands. In comparison with as-deposited films and samples irradiated to low fluence, $MgIn_2O_4$ films implanted with Li^+ ions at high fluence have an over all enhancement in the surface plasmon resonance band, and this is mainly due to the precipitation of lithium nanoparticles in the crystal lattice. This information clearly confirms the presence of a certain percentage of Li^+ ions in the crystal lattice. The strong

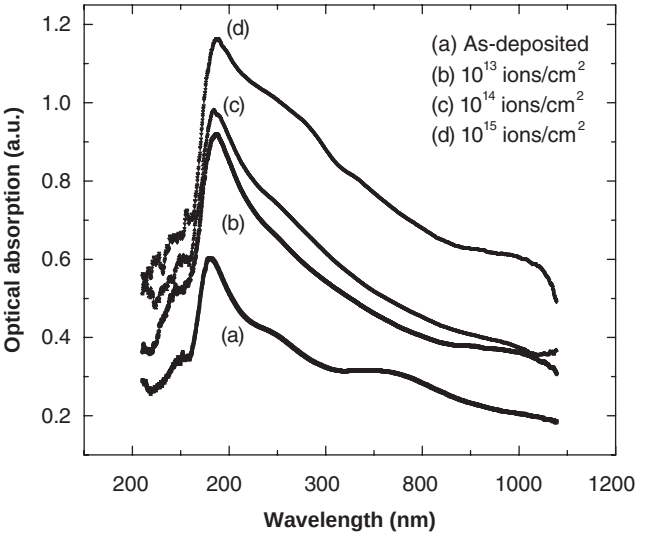

Figure 5. Optical absorption spectra of $MgIn_2O_4$ irradiated with 1.5 MeV Li^+ ions for various fluences.

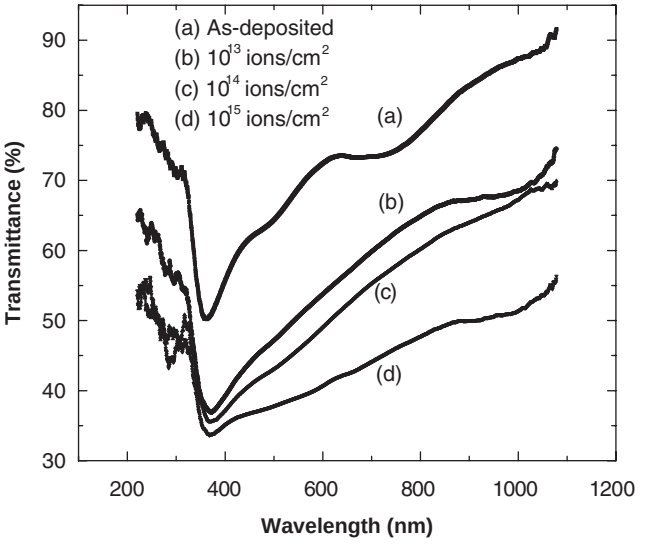

Figure 6. Transmittance spectra of $MgIn_2O_4$ films before and after irradiation with Li^+ ions.

absorption peak at about 365 nm is due to the onset of absorption by free electrons in the conduction band. This strong absorption band can be fitted to a direct band gap model to find the optical band gap energy. The slope of absorption spectra in the wavelength range 300–350 nm suggests the shift in absorption band edge. This shift is termed the Burstein–Moss shift, which may be due to the generation of higher carrier concentration with low effective mass values.

Optical transmission measurements were carried out at room temperature in the wavelength regime from 200 to 1100 nm (Figure 6). The as-deposited films have transmittance in the range of 70–80% in the wavelength range of 400–800 nm. For the Li^+-implanted $MgIn_2O_4$ films, the transmittance is decreased with the increase of ion fluence. $MgIn_2O_4$ films implanted with the highest fluence of 10^{15} ions/cm^2 have transmittance values only in the range between 35% and 45%. The absorption co-efficient α is calculated from the transmittance (T) and thickness of the film (t) using the relation:

$$\alpha = \frac{[\ln(1/T)]}{t}. \tag{1}$$

The absorption co-efficient is in the order of 10^4 cm^{-1} in the visible region and their variations are observed to follow exponential decay with photon energy. From the optical transmission data, the refractive index and extinction co-efficient are evaluated. The index of refraction value of $n = 1.98$ and the extinction co-efficient value of nearly $k = 10^{-2}$ in the visible region are obtained and these values are typical of most spinel TCO materials.

3.4. *Electrical properties*

Electrical conductivity of the Li^+-implanted $MgIn_2O_4$ films was measured as a function of implantation dosage at various temperatures, and the results are shown in Figure 7. The as-deposited $MgIn_2O_4$ films have a very low conductivity, in the order of 10^{-5} S/cm, which may be due to the deficiency of oxygen in the lattice. This result is consistent with a previous report for the $MgIn_2O_4$ films prepared to a thickness of 0.36 μm (*25*). The variations in carrier concentration and mobility may be due to the changes in thickness of the prepared films. However, the conductivity of implanted films to a fluence 10^{15} ions/cm^2 reaches nearly 0.7 S/cm at room temperature.

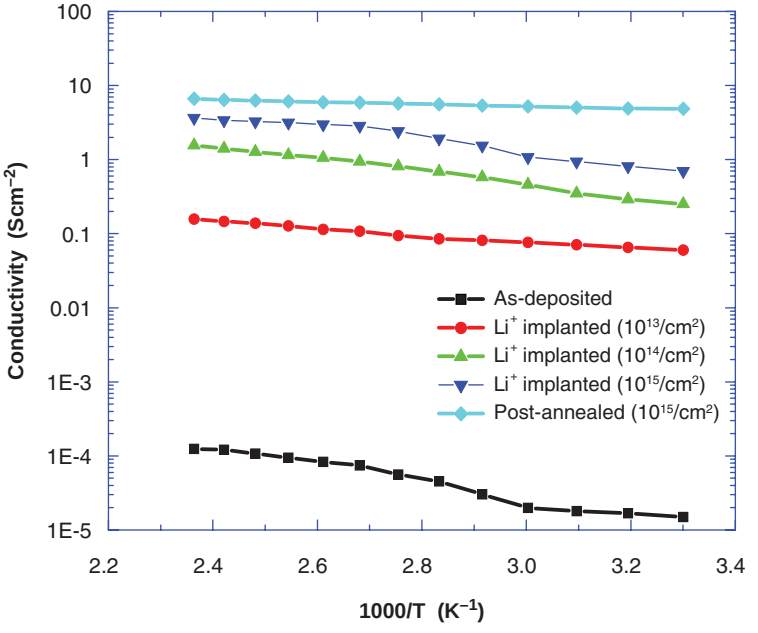

Figure 7. Temperature-dependent conductivity of $MgIn_2O_4$ films implanted with Li^+ ions. Conductivity data of as-deposited and post-annealed films are also shown.

The conductivity therefore increases in the order of five in magnitude after implantation. Annealing the implanted films further increases the electrical conductivity by an order at room temperature. The increase in the electrical conductivity with ion fluence and annealing can be explained on the basis of the inclusion of Li^+ into the lattice and neutralization of charges for electrical conduction. The probable reaction occurred in the lithium-implanted sample for good electrical conduction according to the predictions of Hosono and coworkers (*11*), as follows:

$$Li^+ \xrightarrow{\text{implantation}} Li^+_{\text{lattice}},$$

$$e^- \xrightarrow{\text{neutralization}} e^-_{\text{cond}},$$

where Li^+_{lattice} defines interstitial Li^+ ions and e^-_{cond} refers to the electron introduced from the ground into the conduction band for charge neutralization.

The rise in conductivity with fluence can again be explained on the basis of the knock on process (*26*). In this process, displacement of oxygen ions by a collisional process bearing one or two electrons gives rise to the formation of a donor level and supports the conductivity. In addition, it is predicted that the ionization potential of lithium ions is very low (5.39 eV), and this might be an additional advantage of generating electron carriers by doping Li^+. Many reports are available for $MgIn_2O_4$ films implanted with He^+ (*27*) and no remarkable conductivity changes are observed. The strong evidence for this poor conduction nature is its ionization potential, which is more than five times (*28, 29*) higher than that of Li^+. Moreover, in as-implanted and post-annealed specimens, electrical conductivity is almost independent of temperature.

The effect of Li^+ implantation and post-annealing on $MgIn_2O_4$ films have been further characterized by measuring the carrier concentration and Hall mobility at room temperature by the Van der Pauw method. The results obtained are listed in Table 3. That the sign of the Hall co-efficient is negative for the Li^+ implanted sample indicates that the charge carriers are electrons (n-type conduction). An increase in carrier concentration with fluence revealed the generation of carriers.

Table 3. Carrier concentration, mobility and carrier generation yield in Li^+-implanted and post-annealed $MgIn_2O_4$ films.

Sample details with fluence	Room temperature DC conductivity (S/cm)	Carrier concentration (cm^{-3})	Hall mobility ($cm^2/V\ s$)	Yield (%)
As-deposited	1.5×10^{-5}	8.93×10^{16}	1.05×10^{-3}	–
Li^+ implanted				
10^{13}	0.06	3.125×10^{18}	0.12	13.41
10^{14}	0.25	3.91×10^{18}	0.4	1.68
10^{15}	0.7	4.13×10^{18}	1.06	0.18
Li^+ implanted and post-annealed				
10^{13}	0.13	6.25×10^{18}	0.43	26.81
10^{14}	0.98	7.47×10^{18}	0.82	3.21
10^{15}	4.84	1.03×10^{19}	2.94	0.44

Since the implanted films exhibit degenerate-type semiconducting behavior, the energy levels formed by these electrons generated by implantation is located at positions which are very close to the bottom of the conduction band. Further, the magnitude of Hall mobility is of the order of unity and therefore it supports the band conduction nature (*11*). The efficiency of the carrier generation is increased on annealing the sample irradiated with lower fluences. At higher fluences, the increase in efficiency is not remarkable, indicating the creation of more defect structures on the $MgIn_2O_4$ lattice. So the annealing temperature is insufficient for the complete removal of 'F'-center-type defects. These defects further act as traps for the generated electrons and therefore the carrier generation efficiency decreases with ion dosages.

4. Conclusion

Transparent $MgIn_2O_4$ thin films were successfully deposited on quartz substrates using the chemical spray pyrolysis technique and then implanted with 1.5 MeV Li^+ ions of various fluences ranging 10^{13}–10^{15} ions/cm^2 at room temperature. XRD results revealed an increase in density and unit cell volume. As the implantation doses were increased, a remarkable change in XRD peak intensities and variations in grain size were observed. Micro-structural investigations were conducted on the surface of the implanted $MgIn_2O_4$ films to locate the displacement damages. The macroscopic swelling and shallow pits are evident on the surface of the implanted films. Optical absorption and transmittance spectra were recorded and the effect of implantation on coloration, their disappearance by post-annealing, and absorption bands due to F-centers were analyzed. Conductivity of the films increases with implantation doses, and post-annealing at 450°C gives rise to a slight increase in the conductivity when compared with implanted films. However, the carrier generation efficiency is decreased with ion fluence.

References

(1) Eisen, F.H. *Ion Implantation and Beam Process*; Williams, J.S., Poate, J.M., Eds.; Academic Press: Sydney, 1984.
(2) Chang, S.C.; Yang, Y.; Pei, Q. *Appl. Phys. Lett*. **1999,** *74,* 2081–2083.
(3) Lewis, B.G.; Paine, D.C. *MRS Bull.* **2000,** *25,* 22–27.
(4) Singh, S.P.; Raza, A.; Sharma, A.K.; Agnihotri, O.P.; Thewari, L.M. *Thin Solid Films* **1983,** *105,* 131–138.
(5) Vossen, J.L. *Phys. RCA Rev*. **1971,** *32,* 289–291.
(6) Minemoto, T.; Negami, T.; Nishiwaki, S.; Takakura, H.; Hamakawa, Y. *Thin Solid Films* **2000,** *372,* 173–176.
(7) Zang, Y.; Du, G.; Liu, D.; Zhu, H.; Cui, Y.; Dong, X.; Yang, S. *J. Cryst. Growth* **2004,** *268,* 140–143.
(8) Downs, A.J. Ed. *Chemistry of Aluminium, Gallium, Indium and Thallium*; Springer: Germany, 1993.
(9) Tanji, H.; Kurihara, N.; Yoshida, Y. *J. Mater. Sci. Lett*. **1994,** *13,* 1673–1674.
(10) Paul, A.; Basu, S. *Trans. Br. Ceram. Soc*. **1974,** *73,* 167–172.

(11) Hosono, H.; Un'no, H.; Ueda, N.; Kawazoe, H.; Matsunami, N.; Tanoue, H. *Nucl. Instrum. Methods B* **1995,** *106,* 517–521.
(12) Mryasov, O.N.; Freeman, A.J. *Phys. Rev. B* **2001,** *64,* 233111-1–3.
(13) Wei, S.-H.; Zhang, S.B. *Phys. Rev. B* **2001,** *63,* 045112-1–8.
(14) Korte, C.; Zakharov, N.D.; Hesse, D. *Phys. Chem. Chem. Phys*. **2003,** *5,* 5530–5535.
(15) Moses Ezhil Raj, A.; Som, T.; Ganesan, V.; Jayachandran, M.; Selvan, G.; Swaminathan, V.; Sanjeeviraja, C. *Nucl. Instrum. Methods B* **2008,** *266,* 2564–2571.
(16) Moses Ezhil Raj, A.; Bena Jothy, V.; Ravidhas, C.; Som, T.; Jayachandran, M.; Sanjeeviraja, C. *Radiat. Phys. Chem*. **2009,** *78,* 914–921.
(17) Moses Ezhil Raj, A.; Senthilkumar, V.; Swaminathan, V.; Wollschläger, J.; Suendorf, M.; Neumann, M.; Jayachandran, M.; Sanjeeviraja, C. *Thin Solid Films* **2008,** *517,* 510–516.
(18) Ziegler, J.F.; Biersack, J.P.; Littmark, U. *The Stopping and Range of Ions in Solids;* Pergamon: Oxford, 1985.
(19) Devanathan, R. Yu, N.; Sickafus, K.E.; Nastasi, M. *Nucl. Instrum. Methods B* **1997,** *127–128,* 608–611.
(20) Bordes, N.; Sickafus, K.E.; Cooper, E.A.; Ewing, R.C. *J. Nucl. Mater*. **1995,** 225,318–323.
(21) Sickafus, K.E. *J. Nucl. Mater.* **2003,** *312,* 111–123.
(22) Clinard, F.W. Jr; Hurley, C.F.; Hobbs, L.W. *J. Nucl. Mater*. **1982,** *108/109,* 655–670.
(23) Gosset, D.; Simeone, D.; Dutheil, M.; Bouffard, S.; Beauvy, M. *J. Eur. Ceram. Soc*. **2005,** *25,* 2677–2681.
(24) Kishimoto, N.; Okubo, N.; Plaksin, O.A.; Takeda, Y. *J. Nucl. Mater*. **2004,** *329–333,* 1048–1052.
(25) Moses Ezhil Raj, A.; Selvan, G.; Ravidhas, C.; Jayachandran, M.; Sanjeeviraja, C. *J. Colloid Interface Sci*. **2008,** *328,* 396–401.
(26) Kawazoe, H.; Ueda, N.; Unno, H.; Omata, T.; Hosono, H.; Tanoue, H. *J. Appl. Phys*. **1994,** *76,* 7935–7941.
(27) Un'no, H.; Hikuma, N.; Omata, T.; Ueda, N.; Hashimoto, T.; Kawazoe, H. *Jpn. J. Appl. Phys.* **1993,** *32,* L1260–L1262.
(28) Thomé, L.; Fradin, J.; Jagielski, J.; Gentils, A.; Enescu, S.; Garrido, F. *Eur. Phys. J. Appl. Phys*. **2003,** *24,* 37–48.
(29) Chen, Y.; Abraham, M.M. *J. Phys. Chem. Solids* **1990,** *51,* 747–764.